






Predissociation dynamics of negative-ion resonances of H₂ near 12 and 14.5 eV using the velocity slice imaging technique

Akshay Kumar ¹, Suvasis Swain ^{1,*}, Jankee Upadhyay ², Yogesh Upalekar,¹ Rajesh Arya ², and Vaibhav S. Prabhudesai ^{1,†}

¹Tata Institute of Fundamental Research, Colaba, Mumbai 400005, India

²Laser Electronics Division, Raja Ramanna Centre for Advanced Technology, Indore 452013, India



(Received 25 January 2023; accepted 16 May 2023; published 1 June 2023)

Dissociative electron attachment is an important tool for investigating negative-ion resonances. We have studied the negative-ion resonances of H₂ at 10 and 14 eV using the improved velocity slice imaging technique. We obtained modulations in the kinetic energy spectrum of H⁻ ions obtained at 12 and 14.5 eV electron energy, consistent with the earlier reported vibrational state contributions from the higher-lying bound resonances. We show that structures obtained at 12 eV are due to predissociation of the C²Σ_g⁺ resonance consistent with the current understanding. However, based on our angular distribution measurements, we propose that the structures obtained at 14.5 eV are due to a predissociation of bound resonance of ²Σ_g⁺ symmetry as against Δ_g that was proposed earlier. We also report that the bound ²Σ_g⁺ resonance contributes to the observed inversion symmetry breaking near 14 eV.

DOI: [10.1103/PhysRevA.107.062803](https://doi.org/10.1103/PhysRevA.107.062803)

I. INTRODUCTION

Dissociative electron attachment (DEA) is a useful probe to study negative-ion states. In DEA, the electron is resonantly attached to a molecule to form temporary negative-ion resonances (NIRs), which can dissociate into an anion and one or more neutral fragments. Although electron collisions have been studied for almost a century, many new facets of molecular NIRs have been unraveled recently, thanks to the invention of advanced experimental methods like momentum imaging [1]. For example, only a decade ago, Krishnakumar *et al.* provided reliable values of the experimentally measured absolute cross section of DEA to the simplest molecules, H₂ and D₂, using the momentum imaging technique [2]. Here, velocity slice imaging (VSI), one of the techniques adopted for these measurements, helped to eliminate the contribution from the electronically excited metastable neutrals and ultraviolet light while ensuring the detection of all the ions. These cross sections have provided a benchmark to test the theoretical tools invented [3,4]. From a theoretical aspect, barring a few exceptions, molecular NIRs still need to be successfully modeled. Even for H₂, NIRs are not entirely understood. The observation of quantum coherence in the DEA process in H₂ and D₂ at 14 eV is another example of the new facets of NIRs unraveled by the VSI technique [5]. These results highlighted the role of the ²Σ_u⁺ state at these energies, which has not been identified by any theoretical calculations. On the other hand, Swain *et al.* have shown that from 10.5 eV onwards, the B²Σ_g⁺ negative-ion resonance state of H₂ lies below the

parent b³Σ_u⁺ state [6], which is in contrast with the latest theoretical calculations [7].

H₂ is the simplest molecular system and thus the ideal one to benchmark the theoretical models that describe excited NIRs and their dissociation. Many studies have been carried out on this system in the past few decades [8–10]. DEA to H₂ is of fundamental importance. It leads to the formation of a hydride ion that plays a significant role in the chemistry of the interstellar medium [11–13] and fusion plasmas [14–16]. The H⁻ signal from H₂ in a low-energy regime (<17 eV) comes from three resonant processes [2,17]. The first resonant process occurs around 4 eV via the lowest attractive ground state X²Σ_u⁺ dissociating into H(²S) and H(¹S) [Fig. 1(a)]. This is a threshold process that occurs from the dissociation limit of the ground anion state (3.75 eV). The second resonant process occurs in the 8–13 eV energy range and is associated with the repulsive B²Σ_g⁺ resonant state and leads to H(²S) and H(¹S) products with high kinetic energy (KE) [Fig. 1(a)]. The third resonant process around 14 eV, which was earlier believed to be associated with only the ²Σ_g⁺ resonance [18], is found to be associated with the coherent superposition of two resonant states of ²Σ_g⁺ and ²Σ_u⁺ symmetry, which causes forward-backward asymmetry in the angular distribution [5] [Fig. 1(b)]. The 14 eV peak leads to H⁻(1s²) and H(n = 2) dissociation products. As the dissociation limit for this process is 13.95 eV, the H⁻ is formed with low kinetic energies, similar to that of the 4 eV channel.

The second B²Σ_g⁺ resonance was studied earlier. In the high electron energy resolution experiment, Dowel and Sharp [19] observed structures in H⁻ signal intensity as a function of electron energy in the 11.3–13.3 eV range. Tronc *et al.* [20] have also reproduced these structures. These structures, periodic in electron energy, were in good agreement with the positions of the vibrational levels of resonance series “A” (as per the notation of Schulz *et al.* [21]) observed in the

*Present address: Centre de Recherche sur les Ions, les Matériaux et la Photonique (CIMAP)–UMR 6252–Normandie Université, EN-SCAEN, UNICAEN, CEA, CNRS, 14000 Caen, France.

†vaibhav@tifr.res.in

electron ejection channel [22–24]. This agreement suggests that structures are due to the $C^2\Sigma_g^+(1s\sigma_g)^1(2p\sigma_u)^2$ resonant state. The structures can be understood as arising from the predissociation of the vibrational levels of attractive $C^2\Sigma_g^+$ via the repulsive $B^2\Sigma_g^+$ state [Fig. 1(a)]. Swain *et al.* [6] have observed the effect of $C^2\Sigma_g^+$ resonance in the angular distribution of H^- from H_2 in the 8–13 eV region. However, due to the poor energy resolution of the system, they were unable to get direct evidence of these structures in the ion-yield spectrum.

For the 14 eV peak in the DEA yield, it has been shown that the electron attachment to the ground state ($X^1\Sigma_g^+$) of H_2 leads to a coherent superposition of $^2\Sigma_g^+$ and $^2\Sigma_u^+$ resonant states [5]. It involves the simultaneous transfer of s and p partial waves from the attaching free electron, breaking the inversion symmetry in the system. This symmetry breaking leads to forward-backward asymmetry in the angular distribution of fragment ions. However, in the earlier measurements by Tronc *et al.* [25] with higher electron energy resolution, modulations similar to the 10 eV peak were observed in the H^- ion-yield curve as a function of electron energy [25]. In electron transmission experiments, structures at these energies were identified as “band f ” and were observed by Weingartshofer [26], Golden [27], and Sanchez and Schulz [24]. These authors assigned the $^2\Sigma_g^+$ symmetry for the “ f ” band. However, Tronc *et al.* [25] have assigned Δ_g symmetry for corresponding resonance and proposed that these structures are due to the interaction of Σ_g and Δ_g states through rotations. In this context, it is worthwhile to investigate the features observed at 14 eV using the improved VSI technique, which can show the contribution from the vibrational states of the bound resonance.

The vibrational structures observed in both 10 and 14 eV DEA peaks were obtained using a high-resolution electron beam in the DEA cross-section measurements [20,25]. So far, they have not yet been reported in the momentum-imaging measurements due to the limited electron energy and ion momentum imaging resolution of the apparatus used. In this work, we report these vibrational structures with the improved resolution of momentum imaging set up for both 10 and 14 eV peaks in DEA measurements. Furthermore, using this improved spectrometer, we have obtained details of the symmetry of involved resonances.

II. EXPERIMENTAL SETUP

A magnetically collimated electron beam generated by thermionic emission from the heated tungsten filament was crossed with the effusive molecular beam produced using a capillary array. The electron gun was operated in the pulsed mode (width 100 ns and repetition rate 3000 Hz). The electrons were collected by the Faraday cup situated coaxially at the other end of the interaction zone of the VSI spectrometer. The electron beam was collimated using the magnetic field of 50 G generated using a pair of coils mounted in the Helmholtz geometry outside the vacuum chamber. The interaction volume was spanned by the overlap of the electron, and the molecular beam was situated at the center of the interaction region of the VSI spectrometer. The interaction

region of the spectrometer was flanked by the pusher and puller electrodes separated by 20 mm. The puller electrode has a central aperture of 30 mm lined with a molybdenum wire mesh of 64% transmission. The negative ions formed from electron molecule interaction were extracted into the lens region using a delayed pulsed extraction field. A square voltage pulse of -60 V amplitude and $1\ \mu\text{s}$ duration was used as the extraction pulse on the pusher electrode, which was delayed by 90 ns with respect to the electron pulse. The energy resolution of the electron gun was about 1 eV. The chamber was pumped by oil-free pumps to a base vacuum of 1×10^{-8} Torr. During the experiments, the base pressure of H_2 gas was kept at 3×10^{-6} Torr, and the electron current was 0.36 nA. The energy calibration of the electron beam was carried out by observing the 14 eV peak of H^- from H_2 .

The generated ions were velocity focused via a four-lens assembly [28]. This four-lens assembly allowed the momentum images to be zoomed for low-energy ions to improve the imaging resolution. The ions were detected by a 2D position-sensitive detector (PSD) mounted at the end of the flight tube. The detector was made of two 75-mm-diam active area microchannel plates (MCPs) mounted in the Chevron configuration, followed by a phosphor screen. The images formed on the phosphor screen were recorded by a charge-coupled device (CCD) camera. The VSIs obtained were then analyzed after adding several such slices in the offline analysis.

The detector was kept active only when the central slice of the Newton sphere arrived at it. The appropriate delay of the central slice was obtained by shifting the detector activation window with respect to the pusher pulse and by obtaining the image with the maximum radius. The biasing of the detector was obtained using the Behlke switch having a pulse duration of 10 ns synchronized with the electron pulse with a suitable delay with respect to the pusher pulse. The details of this circuit are given in Appendix A.

The 10 eV resonance dissociates to the same limit as the ground (H_2^-) anion state. The threshold for H^- formation, in that case, is 3.724 eV. This implies that at 12 eV electron energy, the excess energy will appear as the KE of fragments which would be more than 4 eV. Due to low mass and high KE, momentum imaging H^- from H_2 at 10 eV is particularly challenging. The magnetic field applied for electron collimation also adversely affects the H^- imaging. Due to Lorentz force, one side of the Newton sphere moves close to the edge of the lens electrode’s aperture, which results in distortion of momentum images. However, due to cylindrical symmetry around the electron beam, we can use only the other half of the image that passes close to the spectrometer axis to obtain the characteristic dissociation dynamics. In addition, due to the presence of static gas background, it produces an extended source of ions that causes distortions in images [4]. To remove these distorting features, static gas background subtraction was done by diverting the gas flow through another entrance and keeping the base pressure the same.

The energy resolution of the momentum image is directly related to the annular width of the obtained image. The annular width depends upon the velocity focusing conditions, time-slicing width, and the electron’s energy resolution width (Appendix B). To determine the focusing conditions, the

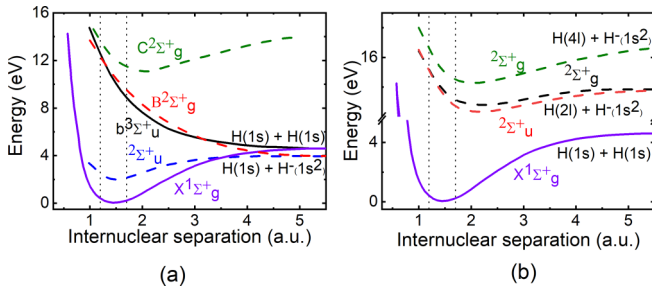


FIG. 1. Schematic potential energy curves of the neutral H₂ (solid lines) and H₂⁻ (dashed lines) relevant to DEA around (a) 12 eV and (b) 14.5 eV. The dotted line indicates the Franck-Condon region.

potentials on various electrodes were estimated using SIMION simulations (Appendix C). The electrode voltages were further fine-tuned in the experiment to obtain the best achievable velocity-focusing condition. The small slicing width can reduce the contribution of the noncentral part of the Newton sphere (i.e., from the ions with the initial momentum vector not in the plane containing the electron beam momentum) and thus can help in improving the energy resolution of the image. Poor electron energy resolution has an advantage for H₂. As a diatomic molecule, on dissociation from a particular resonance, excess energy above the threshold of the process would appear as the fragment's KE. We can access the different parts of the ion yield curve over the energy spread in the electron beam by fixing the mean electron's energy at a particular value. We used SIMION to obtain the expected energy resolution of the momentum image for a specific set of the initial kinetic energies and with the other conditions matching the experimental scheme. The effect of the thermal motion of particles from an effusive jet having an aspect ratio of 10 at room temperature, 1 cm from the end of the capillary array, and dissociating in random directions in the interaction region was estimated. It was found that the thermal motion was adding to the energy width by about 25 meV. This spread of energy was incorporated into the SIMION simulations. The ions were flown, and the Newton sphere was time-sliced in a separate analysis. The annular width of the obtained image

is used to determine the corresponding momentum resolution of the imaging condition. Due to the presence of the magnetic field, the image loses the cylindrical symmetry about the spectrometer axis. As a result, energy resolution was found to be angle-dependent. This effect is more pronounced for high KE ions. For 4 eV, H⁻ ion energy resolution is found to be 80 meV near 30°–60° and around 90 meV around 40°–70° with respect to incident electron direction for 10 ns time gating and about 300 meV for 80 ns time gating.

To compare our data with those from Tronc *et al.* [20], we multiplied their reported cross-section data with the electron gun profile of our experiment and convoluted the result with an obtained energy resolution of the imaging spectrometer. Figure 2 shows the importance of 10 ns time gating compared to 80 ns time gating. Despite poor electron energy resolution, we could observe the effect of the vibrational structures in KE distribution in the 10 ns slicing due to good imaging resolution.

The VSI condition was modified to map the low-energy H⁻ ions obtained at 14.5 eV with appropriate magnification. Under that lensing condition, SIMION simulations were carried out to determine the imaging resolution of the spectrometer. After a similar analysis to that done for 4 eV H⁻ ions, we found energy resolution for 0.3 eV H⁻ ions to be around 60 meV in all angular ranges. To obtain the expected KE distribution, we multiplied the observed ion-yield data of Tronc *et al.* [25] with the electron gun profile and convoluted the result with the 60 meV energy resolution of the imaging spectrometer. The obtained spectrum is shown in Fig. 2(c). For the ions with initial KE close to zero, the image would appear as a filled region at the center. We call it a “blob.” The intensity of such a distribution in the slice image is artificially enhanced compared to higher-energy ions due to the geometry factor arising from the finite width of the parallel slice. Such a slice gives an intrinsic bias towards the low-energy ions as all of them are detected, whereas for the higher-energy ions, depending on their spread in the time of flight, only a limited part is imaged spread over a larger area. Hence, the simulated KE distribution obtained after multiplying the data from Tronc *et al.* near 14 eV [25] with the electron gun profile needed to be multiplied by an additional weight factor that depends on the overall spread of the time-of-flight peak against the

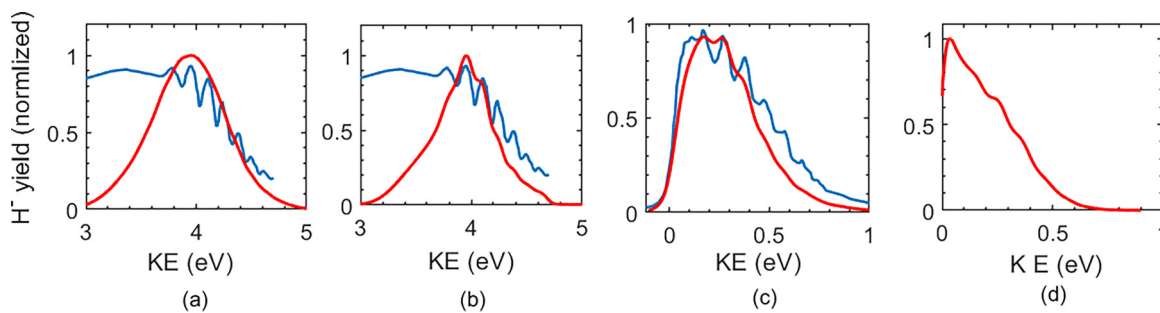


FIG. 2. (a) KE distribution of H⁻ (solid red line) at incident energies near 12 eV obtained by multiplying historic ion yield data (solid blue line) from Ref. [20] with the electron beam profile centered around 12 eV, and convoluting the product with an imaging resolution of 300 meV expected from time gating at 80 ns. (b) Same as (a) but convoluting with a 90 meV imaging resolution associated with 10 ns time gating. (c) Expected KE distribution of H⁻ (solid red line) near 14.5 eV obtained having multiplying the ion-yield data (solid blue line) from Ref. [25] with an electron beam profile, centered around 14.5 eV and convoluting the product with a 60 meV imaging resolution. (d) Expected KE distribution of H⁻ near 14 eV after taking into account the weight factor (see the text).

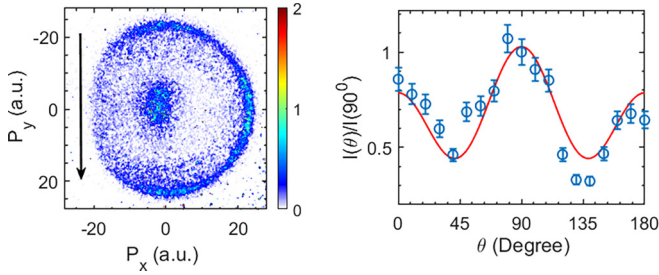


FIG. 3. (a) Background subtracted momentum image of H^- from H_2 obtained at 12 eV electron energy. The color bar indicates the ion intensity in arb. units. The direction of the electron beam is from top to bottom, as indicated by the black arrow. (b) The angular distribution of the ions in the KE range of 3.8–4.2 eV and the corresponding fitting of angular distribution is also shown (solid red line). The angular distribution is normalized at 90° .

width of the slicing. After multiplying the weight factor and convoluting it with 60 meV imaging resolution, the modified KE distribution is shown in Fig. 2(d).

III. RESULTS AND DISCUSSION

For a homonuclear diatomic molecule, due to the presence of inversion symmetry in the system, electron capture proceeds through the transfer of either odd or even partial waves [29]. Under the axial recoil approximation, the angular preference during electron capture will be mapped in the angular distribution of dissociation products. The general form of the angular distribution [30] of the molecule is given by

$$I(k, \theta, \varphi) = \left| \sum_{l=m}^{\infty} A_{lm}(k) Y_{lm}(\theta, \varphi) \right|^2, \quad (1)$$

where A_{lm} is the transition amplitude between the target state and the resonant state, l is the orbital angular momentum of the incident electron, and m is the difference between the electronic axial angular momenta of the target state and the resonant state. $Y_{lm}(\theta, \varphi)$ are the corresponding spherical harmonics involved, angle θ represents the angle of ejection of an anion fragment with respect to the incident electron beam, and φ is the corresponding azimuthal angle.

A. Predissociation near 12 eV

The experimentally obtained momentum image for the H^- ions from H_2 at 12 eV after background subtraction is shown in Fig. 3(a). At 12 eV, the blob seen in the center of the image is due to the long energy tail of the electron beam, which produces negative ions from the 14 eV resonance. The observed shift of the blob away from the center is due to the effect of the magnetic field used for electron beam collimation [6]. This is consistent with the simulations carried out with the charged-particle trajectory simulation program: SIMION 8.2. The thin ring obtained is from the 4 eV ions formed from the DEA via $B^2\Sigma_g^+$ resonance. The effect of thin slicing of 10 ns can be seen in the annular width of the ring as compared to earlier 80 ns slicing [6]. Near 12 eV, the transition occurs between the $X^1\Sigma_g^+$ state of H_2 to the repulsive $B^2\Sigma_g^+$ and bound $C^2\Sigma_g^+$ states of H_2^- [19]. According to the selection rule of the $g \rightarrow g$ transition, only even partial waves are allowed. At low energy, lower allowed partial waves have a dominant contribution to the capture.

Therefore, at 12 eV, the contribution from only s and d partial waves of the electron would suffice to describe the angular distribution. A similar analysis will also hold after including the contribution from the bound $C^2\Sigma_g^+$ resonance. The angular distribution from the corresponding transition can be expressed as

$$I(k, \theta) = |A_{00}(k)Y_{00}(\theta, \varphi) + A_{20}(k)Y_{20}(\theta, \varphi)e^{-i\delta}|^2, \quad (2)$$

which on solving gives

$$I(k, \theta) = \frac{A_{00}^2(k)}{4\pi} + 5\frac{A_{20}^2(k)}{16\pi}(3\cos^2\theta - 1)^2 + \sqrt{5}\frac{A_{00}(k)A_{20}(k)}{4\pi}(3\cos^2\theta - 1)\cos(\delta). \quad (3)$$

Here A_{00} and A_{20} are transition amplitudes corresponding to the attachment of s and d waves of the incident electron, respectively, and δ is the relative phase between two partial waves.

Using Eq. (3), the angular distribution obtained for the momentum image [Fig. 3(a)] is fitted. The corresponding fitted curve is shown by the solid red line in Fig. 3(b). Using the fitted parameters, the ratio of transition amplitudes (A_{00}/A_{20})

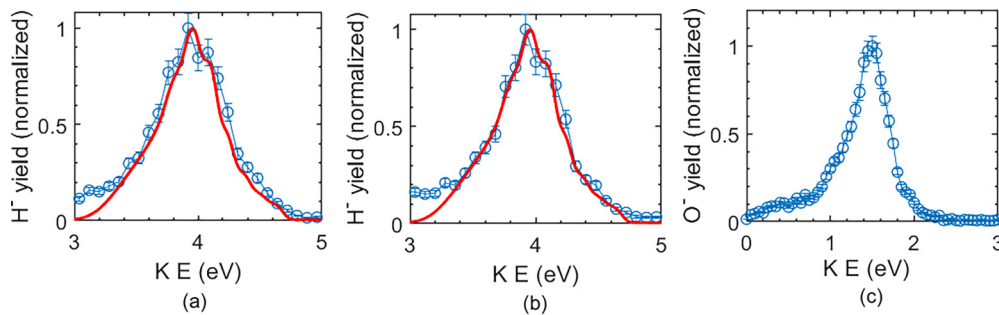


FIG. 4. KE distribution of H^- from H_2 obtained at 12 eV electron energy in the angular range of (a) 40° – 70° and (b) 30° – 60° using time slicing of 10 ns. The effect of thin slicing can be seen in vibrational structures in the ion-yield spectrum. The ion-yield curve obtained after multiplying the data from Tronc *et al.* [20] with the electron gun profile and convoluting it with imaging resolution (see the text) is also shown in a solid red line. (c) KE distribution of O^- from O_2 obtained around 6.5 eV electron energy around 90° using time slicing of 10 ns and the same spectrometer operating condition.

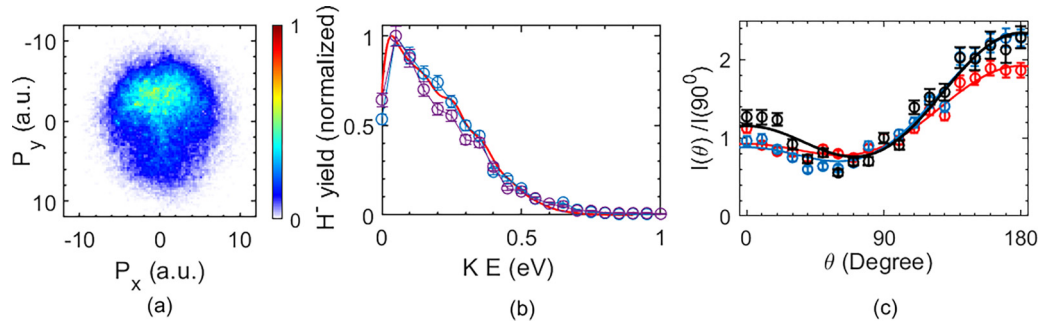


FIG. 5. (a) Background subtracted momentum image of H^- from H_2 obtained at 14.5 eV electron energy using the 10 ns time slice. The color bar indicates the ion intensity in arb. units. The direction of the electron beam is from top to bottom. (b) Corresponding KE distribution obtained in the angular range of $75^\circ-105^\circ$ (blue circles) and $40^\circ-70^\circ$ (violet circles). The solid red line shows the expected KE distribution shown in Fig. 2(d). (c) A comparison of the angular distribution obtained from the image and normalized at 90° in the KE range of 0–0.15 eV (red circles), where we expect no vibrational structures with the KE ranges of 0.15–0.3 eV (blue circles) and 0.3–0.45 eV (black circles), where we expect vibrational structures. The solid lines show the corresponding fits.

is calculated, and the ratio is found to be 1.82 ± 0.3 , which is consistent with earlier reported results from the higher electron energy resolution experiment by Tronc *et al.* [20]. The increased s/d ratio around 12 eV is explained due to an additional contribution from the resonance of identical symmetry ($C^2\Sigma_g^+$) [6].

To see the effects of $C^2\Sigma_g^+$ resonance on the ion-yield spectrum, KE distribution of H^- ions was plotted in the region where the contribution due to the d wave is minimum, i.e., around 55° . The obtained KE distribution for the 12 eV images in the $40^\circ-70^\circ$ angular region is shown in Fig. 4(a). The corresponding expected KE distribution from Fig. 2(b) is also shown as the solid red line. The presence of vibrational structure can be seen as shoulders at 3.8 and 4.2 eV, which correspond to peaks coming at 11.3 and 11.9 eV, respectively, in the ion-yield curve reported by Tronc *et al.* [20]. Similar effects can be seen for KE distribution plotted in a $30^\circ-60^\circ$ angular region for which the best energy resolution is expected (80 meV), as shown in Fig. 4(b). The counts below 3.5 eV were generated due to the remaining background contribution. To verify that these structures are not from any experimental artifact, we obtained the VSI image of O^- from O_2 using 10 ns slicing. For O_2 , we do not expect any structures in the KE spectrum. As shown in Fig. 4(c), the obtained KE spectrum of O^- from O_2 is free from any structures and thus verifies that the structures observed in H_2 are not imaging artifacts.

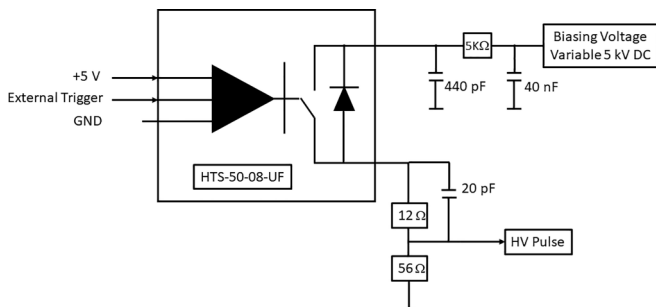


FIG. 6. Block diagram of the high-voltage pulse generator unit.

B. Predissociation near 14 eV

After obtaining the earlier reported vibrational structure in the KE distribution at 12 eV, we carried out similar measurements for the 14 eV peak. Since the KE of H^- at 14.5 eV is <0.7 eV, the corresponding VSI image is a blob, as shown in Fig. 5(a). The energy calibration is carried out from a similar image recorded at 15 eV. The corresponding KE distribution is shown in Fig. 5(b), along with the expected curve from Fig. 2(d). Previously, the 14 eV resonance was believed to be associated uniquely with $^2\Sigma_g^+$, but recently it was shown that 14 eV resonance is associated with both $^2\Sigma_g^+$ and $^2\Sigma_u^+$ resonance. Thus, structures observed around 14 eV in principle can come from the interaction of both resonances with another high-lying bound resonance. To check the involvement of the resonances, the KE distribution of H^- for the 14.5 eV electron energy image was obtained around the 90° angular region with respect to the incoming electron beam direction and is plotted in Fig. 5(b).

Since the contribution of $^2\Sigma_u^+$ is minimum around 90° , the presence of vibrational structures shows that the latter must arise from the interaction of $^2\Sigma_g^+$ with another bound resonance. Tronc *et al.* [25] have also observed the structures around 90° , and it was proposed that these structures are due

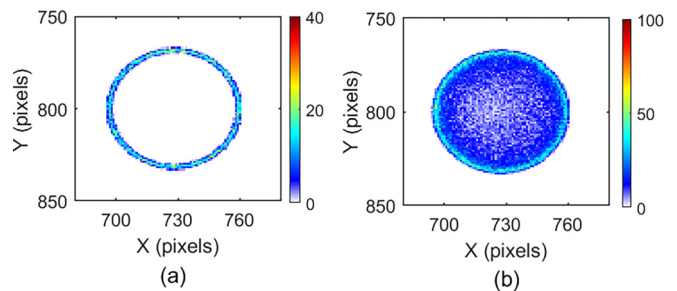


FIG. 7. The velocity slice image obtained for 0.3 eV H^- ions. Pusher = -50 V (pulsed), puller = 0 V, $L1 = -15$ V, $L2 = 250$ V, $L3 = 150$ V, $L4 = 250$ V, FT = 300 V, MCP front = 600 V lensing conditions, after (a) 10 ns and (b) 80 ns time gating near the central slice. The color bar indicates the ion counts.

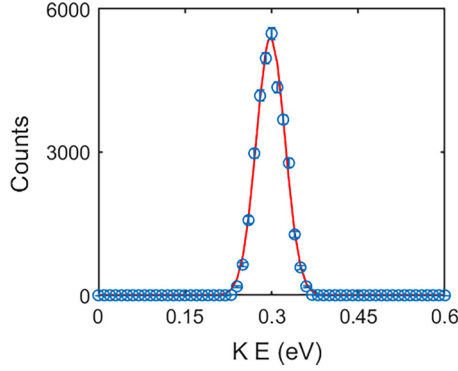


FIG. 8. KE spectrum (blue circles) of 10 ns time-sliced simulated image obtained for 0.3 eV H^- ions with the voltage conditions: Pusher = -50 V (pulsed), puller = 0 V, $L1 = -15$ V, $L2 = 250$ V, $L3 = 150$ V, $L4 = 250$ V, FT = 300 V, MCP front = 600 V. The corresponding KE spectrum is fitted with a Gaussian curve (solid red line).

to the interaction of $^2\Sigma_g^+$ with $^2\Delta_g$ state through rotational coupling.

To determine the symmetry of the bound resonance, we have plotted the angular distribution in different KE ranges. KE distribution has no structures for $0-0.15$ eV, as shown in Fig. 5(b). The angular distribution in this region would be due to the capture of only s and p partial waves of a free electron coming from transition $X^1\Sigma_g^+ \rightarrow ^2\Sigma_g^+$ and $X^1\Sigma_g^+ \rightarrow ^2\Sigma_u^+$, respectively. The expected angular distribution can be expressed [31] as

$$I(k, \theta) = |A_{00}(k)Y_{00}(\theta, \varphi) + A_{10}(k)Y_{10}(\theta, \varphi)e^{-i\delta}|^2, \quad (4)$$

$$I(k, \theta) = A_{00}^2(k) + 3A_{10}^2(k)\cos^2\theta + 2\sqrt{3}A_{00}(k)A_{10}(k)\cos(\theta)\cos(\delta), \quad (5)$$

where A_{00} and A_{10} are transition amplitudes corresponding to the attachment of the s wave and p wave of the incident electron, respectively, and δ is the sum of the relative phase gained during the dissociation along the two paths and the initial relative phase between the s and p waves. The presence of the $\cos(\theta)$ term will induce forward-backward asymmetry in the angular distribution.

Electron capture from the $X^1\Sigma_g^+$ state of H_2 to the Δ_g resonant state requires the capture of the d wave of a free electron. However, the angular distribution shown in Fig. 5(c) obtained for $0.15-0.3$ and $0.3-0.45$ eV is similar to the $0-0.15$ eV KE range and could be fitted to Eq. (5). Obtained fitted parameters for angular distribution in different KE ranges are shown in Table I. This indicates that there is no involvement of the d

TABLE I. Transition amplitudes and relative phase from the angular distributions H^- from H_2 at 14.5 eV electron energy in different KE ranges.

| KE range (eV) | A_{00} | A_{10} | δ (rad) |
|---------------|-----------------|-----------------|-----------------|
| 0–0.15 | 0.94 ± 0.07 | 0.42 ± 0.08 | 4.34 ± 0.10 |
| 0.15–0.3 | 0.94 ± 0.04 | 0.49 ± 0.05 | 4.24 ± 0.06 |
| 0.3–0.45 | 0.93 ± 0.08 | 0.54 ± 0.06 | 4.36 ± 0.06 |

TABLE II. Comparison of measured asymmetry parameter (η) in different KE ranges of H^- from H_2 at 14.5 eV electron energy.

| KE range (eV) | Experimental values of η |
|---------------|-------------------------------|
| 0–0.15 | -0.31 ± 0.02 |
| 0.15–0.3 | -0.38 ± 0.02 |
| 0.3–0.45 | -0.35 ± 0.02 |

wave in the angular distribution; hence, we can conclude that the Δ_g state does not contribute directly to the DEA signal.

Moreover, the contribution of the d partial wave is minimum around 55° if the bound resonance is of Δ_g symmetry. Hence, we should not expect any structures in KE distribution around 55° . On the contrary, we have observed structures in KE distribution in the form of shoulders appearing at the $0.15-0.3$ eV KE range and the $0.3-0.45$ eV KE range around 55° similar to structures observed around 90° , as shown in Fig. 5(b). The corresponding KE distribution is also compared with the simulated distribution [Fig. 2(d)] and is shown by the solid red line in Fig. 5(b). This also eliminates the possibility of the higher-lying bound resonance of the Δ_g symmetry directly contributing to the DEA signal. Sanchez and Schulz have also observed 14 eV structures in the electron scattering experiment, and they assigned Σ_g symmetry to the corresponding resonance. From these observations, we conclude that the vibrational structures observed in the ion yield of the 14 eV resonance are arising due to the interaction of $^2\Sigma_g^+$ resonance with another high-lying bound resonance of $^2\Sigma_g^+$ symmetry. Using the energy values where Tronc *et al.* [25] have gotten the structures in the 14 eV region and comparing them with vibrational states [32] of H_2 , we propose that the high-lying bound $^2\Sigma_g^+$ resonance originates from the $D^1\Pi_u$ state with dissociation limit $H + H(n=4)$ of H_2 as the parent state [33]. This assignment also provides a much simpler explanation of the vibrational features observed on the lines similar to those for the 12 eV signal without invoking any rotational coupling between the two resonances of different symmetries.

To observe the effect of the bound $^2\Sigma_g^+$ resonance that is causing structures in the 14 eV region on the symmetry breaking, we have determined the asymmetry parameter [31] of the velocity slice image obtained at 14.5 eV in different KE ranges, as shown in Table II. From earlier calculations [5], it was shown that if we consider only $^2\Sigma_g^+$ and $^2\Sigma_u^+$ dissociating resonances, the energy-integrated asymmetry parameter decreases with electron energy beyond 14 eV. On the other hand, if bound $^2\Sigma_g^+$ resonance contributes incoherently to the DEA process, the asymmetry parameter should decrease in the $0.15-0.45$ eV KE range where there is a contribution from the bound $^2\Sigma_g^+$. But from Table II, it can be seen that the involvement of the bound $^2\Sigma_g^+$ state is causing an increase in asymmetry. This shows that high-lying $^2\Sigma_g^+$ resonance is coherently participating in the symmetry-breaking process observed near 14 eV. However, the contribution from the bound resonance does not diminish the anisotropy and the forward-backward asymmetry. This finding also supports the assignment of the bound resonance as a $^2\Sigma_g^+$ state, as any rotational coupling would smear the anisotropy and hence the

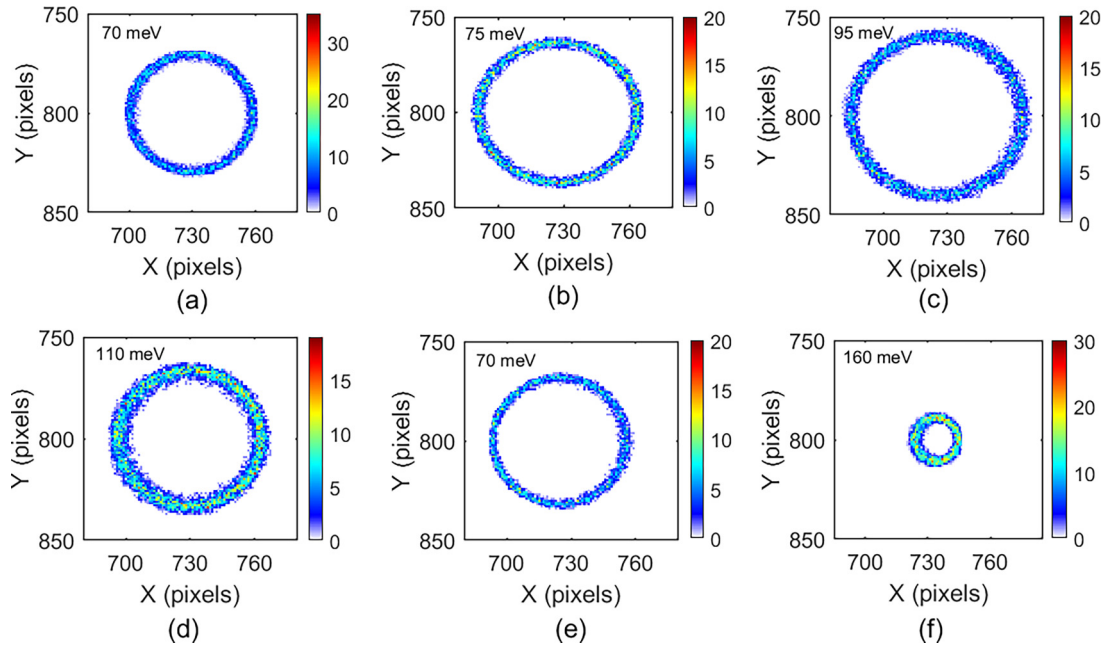


FIG. 9. Simulated image obtained for 0.3 eV H^- , $L2 = 250$ V, $L3 = 150$ V, $L4 = 250$ V, $FT = 300$ V, MCP front = 600 V. (a) Pusher = -50 V, $L1 = -30$ V. (b) Pusher = -50 V, $L1 = 0$ V. (c) Pusher = -50 V, $L1 = 15$ V. (d) Pusher = -70 V, $L1 = -15$ V. (e) Pusher = -30 V, $L1 = -15$ V. (f) Pusher = -30 V, $L1 = -70$ V lensing conditions. The corresponding energy resolution is written inside the images. The color bar indicates the ion counts.

asymmetry. It is also important to note that the next dissociation limit available for the DEA process, namely $H(n=3) + H^{-1}(^1S)$, is at 15.86 eV [34], which is just about at the edge of the energy spread of the electron beam at 14.5 eV. However, the measured cross section at this energy is very small [2]. Consequently, this channel will have a negligible contribution to the signal in the KE range of 0–0.15 eV and will not influence the inference.

IV. CONCLUSION

Using a VSI spectrometer with improved energy resolution due to 10 ns time slicing, we have observed the effect of vibrational structures at 12 and 14.5 eV electron energy in the KE distribution of H^- ions from H_2 . These structures are consistent with the earlier reports by Tronc *et al.* [20,25]. At 12 eV, the structures are due to a predissociation of a bound $C^2\Sigma_g^+$ resonance state via the repulsive $B^2\Sigma_g^+$ resonance. The main contribution to the repulsive resonance is from the transfer of s and d partial waves to the target molecule. The bound resonance contributes predominantly to the s wave capture. At 14.5 eV, we identify the structures in the KE distribution of ions as due to the predissociation of $^2\Sigma_g^+$ bound resonance in contrast to the earlier proposed $^2\Delta_g$ resonance state. We infer this from the angular distributions obtained at various KE ranges and by obtaining the KE distributions in various angular ranges, ruling out the contribution of the d partial wave. We propose that this bound resonance of $^2\Sigma_g^+$ symmetry may have the $D' \ ^1\Pi_u$ state of neutral H_2 as the parent state. We also propose that this upper bound resonance contributes to the symmetry breaking of the inversion symmetry as its contribution should be added coherently to the resultant transition.

ACKNOWLEDGMENTS

S.S., A.K., and V.S.P. acknowledge the financial support from the Department of Atomic Energy, India, under Project Identification No. RTI4002. All authors acknowledge S.V. Nakhe for support, and Sudhir Kumar for help in the fabrication of the pulse generator.

APPENDIX A

The Behlke switch-based pulse generator is specifically developed for the experimental setup. The requirement was to generate a high-voltage (HV) pulse of 2.5 kV with a pulse duration of 10 ns and a switching time of better than 2 ns at an adjustable repetition rate of more than 1 kHz. There are several techniques for achieving HV fast switching [35–37] based on switches realized by using transistors, metal-oxide semiconductor field-effect transistors, insulated gate bipolar transistors, etc. In the present work, the pulse generator has been developed using a Behlke solid-state HV switch (HTS-50-08-UF). These solid-state switches are specially designed and developed to generate HV pulses of a short duration of 10 ns and a constant fast rise time better than 2 ns. These switches, being semiconductor devices, have a very low turn-on jitter of the order of 100 ps and a longer lifetime. These switches can provide galvanic isolation of more than 10 kV, thus they can be floated at the required high potential and used as high-side switches for positive as well as negative voltages.

The block diagram of the pulse generator is shown in Fig. 6. It has been realized by charging a 440 pF/6 kV capacitor to the desired voltage and discharging into a load resistance of matched impedance using HV switching in synchronization with an external trigger signal. The discharging current

generates an HV pulse of half the applied biasing voltage with a duration of 10 ns fixed for the selected Behlke switch. The pulse amplitude can be varied by varying the applied biasing voltage. High-speed switching often leads to various difficulties, including self-oscillating, self-retriggering, ringing, etc. To overcome these difficulties, a printed circuit board (PCB) layout has been designed by minimizing the value of parasitic reactive components, matching the load with output impedance, and implementing the star grounding scheme. EMI shielding of the pulser circuit has been achieved by specifically designed and fabricated enclosure of size 220 mm \times 110 mm \times 185 mm using a 3 mm MS Ni-chromium plated sheet.

APPENDIX B

The VSI spectrometer consists of two electrodes, a pusher and a puller, separated by 20 mm. These two electrodes are followed by fourfold electrostatic lens assembly ($L1$, $L2$, $L3$, $L4$), a flight tube (FT), and an MCP detector [28]. Velocity focusing conditions are mainly decided by the pusher and $L1$ voltages. Lensing conditions used in the experimental image of the low-energy ions generated at 14.5 eV electron energy are pusher = -50 V (pulsed), puller = 0 V, $L1 = -15$ V, $L2 = 250$ V, $L3 = 150$ V, $L4 = 250$ V, FT = 300 V, MCP front = 600 V. The ions were generated in a spherical region of radius 1 mm at the center of the interaction region. The initial uncertainty of the ion generation is 100 ns, which matches the electron pulse width. The initial velocity distribution of the

ions is isotropic, with a KE of 0.3 eV. The extraction voltage, i.e., the voltage on the pusher, is applied with a delay of 80 ns from the ion-generation window. The extraction pulse on the pusher is of 1 μ s duration with a rise and fall time of 10 ns that matches the voltage pulses used in the experiment. In the simulations, we obtained the positional and time information for each hit on the detector. We use position information of only those ions that arrive in the desired slice window in time. After analyzing the output data, the corresponding image can be obtained. Figure 7 shows the image obtained for 10 and 80 ns time gating near the central slice for H^- ions.

Although the initial KE of the ions has a fixed value, the image shows a radial distribution. This distribution is calibrated for the conversion to KE, giving the energy distribution in the sliced image. The KE spectrum is plotted for the image in Fig. 8, and the corresponding spectrum is fitted with a Gaussian. The FWHM of the fitted curve is taken as the imaging energy resolution.

A similar analysis is done for 80 ns time-sliced images, giving 190 meV imaging energy resolution. This imaging resolution changes with the mean KE. The optimized resolution for 4 eV KE is found to be 300 meV from the 80 ns slice.

APPENDIX C

Imaging resolution depends on the operating conditions. Figure 9 shows the simulated 10 ns sliced images for different operating conditions. The corresponding nearby resolution is also written inside the images.

-
- [1] D. Nandi, V. S. Prabhudesai, A. Chatterjee, and E. Krishnakumar, *Rev. Sci. Instrum.* **76**, 053107 (2005).
 - [2] E. Krishnakumar, S. Deniff, I. Čadež, S. Markelj, and N. J. Mason, *Phys. Rev. Lett.* **106**, 243201 (2011).
 - [3] R. Celiberto, R. K. Janev, V. Laporta, J. Tennyson, and J. M. Wadehra, *Phys. Rev. A* **88**, 062701 (2013).
 - [4] V. Laporta, R. Agnello, G. Fubiani, I. Furno, C. Hill, D. Reiter, and F. Taccogna, *Plasma Phys. Control. Fusion* **63**, 085006 (2021).
 - [5] E. Krishnakumar, V. S. Prabhudesai, and N. J. Mason, *Nat. Phys.* **14**, 149 (2018).
 - [6] S. Swain, E. Krishnakumar, and V. S. Prabhudesai, *Phys. Rev. A* **103**, 062804 (2021).
 - [7] D. T. Stibbe and J. Tennyson, *J. Phys. B* **31**, 815 (1998).
 - [8] N. Bardsley, A. Herzenberg, and F. Mandl, *Proc. Phys. Soc.* **89**, 305 (1966).
 - [9] J. Horáček, M. Čížek, K. Houfek, P. Kolorenč, and W. Domcke, *Phys. Rev. A* **70**, 052712 (2004).
 - [10] J. N. Bardsley and J. S. Cohen, *J. Phys. B* **11**, 3645 (1978).
 - [11] H. Kreckel, H. Bruhns, M. Čížek, S. C. O. Glover, K. A. Miller, X. Urbain, and D. W. Savin, *Science* **329**, 69 (2010).
 - [12] D. Field, *Astron. Astrophys.* **362**, 774 (2000).
 - [13] S. C. Glover, D. W. Savin, and A.-K. Jappsen, *Astrophys. J.* **640**, 553 (2006).
 - [14] U. Fantz, D. Reiter, B. Heger, and D. Coster, *J. Nucl. Mater.* **290-293**, 367 (2001).
 - [15] F. Taccogna, R. Schneider, K. Matyash, S. Longo, M. Capitelli, and D. Tshakaya, *Contrib. Plasma Phys.* **48**, 147 (2008).
 - [16] M. Bacal and M. Wada, *Appl. Phys. Rev.* **2**, 021305 (2015).
 - [17] D. Rapp, T. E. Sharp, and D. D. Briglia, *Phys. Rev. Lett.* **14**, 533 (1965).
 - [18] A. Weingartshofer, H. Ehrhardt, V. Hermann, and F. Linder, *Phys. Rev. A* **2**, 294 (1970).
 - [19] J. T. Dowel and T. E. Sharp, *Phys. Rev.* **167**, 124 (1968).
 - [20] M. Tronc, C. Schermann, R. I. Hall, and F. Fiquet-Fayard, *J. Phys. B* **10**, 305 (1977).
 - [21] G. J. Schulz, *Rev. Mod. Phys.* **45**, 378 (1973).
 - [22] C. E. Kuyatt, J. A. Simpson, and S. R. Mielczarek, *J. Chem. Phys.* **44**, 437 (1966).
 - [23] G. Joyez, J. Comer, and F. H. Read, *J. Phys. B* **6**, 2427 (1973).
 - [24] L. Sanche and G. J. Schulz, *Phys. Rev. A* **6**, 69 (1972).
 - [25] M. Tronc, R. I. Hall, C. Schermann, and H. S. Taylor, *J. Phys. B* **12**, L279 (1979).
 - [26] H. Ehrhardt and A. Weingartshofer, *Z. Phys.* **226**, 28 (1969).
 - [27] D. E. Golden, N. F. Lane, A. Temkin, and E. Gerjuoy, *Rev. Mod. Phys.* **43**, 642 (1971).
 - [28] K. Gope, V. Tadsare, V. S. Prabhudesai, and E. Krishnakumar, *Eur. Phys. J. D* **71**, 323 (2017).
 - [29] T. F. O'Malley and H. S. Taylor, *Phys. Rev.* **176**, 207 (1968).

- [30] R. J. Van Brunt and L. J. Kieffer, *Phys. Rev. A* **2**, 1899 (1970).
- [31] V. S. Prabhudesai, N. J. Mason, and E. Krishnakumar, *J. Phys.: Conf. Ser.* **1412**, 052006 (2020).
- [32] T. Namioka, *J. Chem. Phys.* **41**, 2141 (1964).
- [33] T. E. Sharp, *Atom. Data Nucl. Data Tables* **2**, 119 (1971).
- [34] NIST Chemistry Webbook, <https://webbook.nist.gov/chemistry>, accessed on 21 April, 2023.
- [35] J. Upadhyay, M. L. Sharma, C. P. Navathe, M. A. Toley, S. J. Shinde, S. A. Nadkarni, and S. K. Sarkar, *Rev. Sci. Instrum.* **83**, 024709 (2012).
- [36] J. Upadhyay and C. P. Navathe, *Meas. Sci. Technol.* **17**, N25 (2006).
- [37] R. J. Baker and B. P. Johnson, *Rev. Sci. Instrum.* **64**, 1655 (1993).